Paleostress magnitudes in folded sedimentary rocks

Khalid Amrouch,[1,2,3] Nicolas Beaudoin,[1,3] Olivier Lacombe,[1,3] Nicolas Bellahsen,[1,3] and Jean-Marc Daniel[2]

[1]   Using Sheep Mountain Anticline (Wyoming, USA) as a case study, we propose a new approach to quantify effective paleo-principal stress magnitudes in the uppermost crust. The proposed mechanical scenario relies on a well-documented kinematic and chronological sequence of development of faults, fractures and microstructures in the folded strata. Paleostress orientations and regimes as well as differential stress magnitudes based on calcite twinning paleopiezometry are combined with rock mechanics data in a Mohr construction to derive principal stress magnitudes related to the successive steps of layer-parallel shortening and to late stage fold tightening. Such quantification also provides original insights into the evolution of the fluid (over)pressure and amount of syn-folding erosion. **Citation:**   Amrouch, K., N. Beaudoin, O. Lacombe, N. Bellahsen, and J.-M. Daniel (2011), Paleostress magnitudes in folded sedimentary rocks, *Geophys. Res. Lett.*, *38*, L17301, doi:10.1029/2011GL048649.

1.   Introduction

[2]   Quantitative estimates of stresses and strength are central to many problems of crustal mechanics. To date however, our knowledge of the stress levels sustained by tectonically deformed rocks remains poor. Present-day stresses measured *in situ* reflect local, instantaneous crustal stresses and it is difficult to unambiguously relate their magnitudes to ongoing tectonic deformation. Thus, paleostresses reconstructed from the study of tectonic structures may have a greater potential to reflect ancient crustal stresses at the particular time of tectonic deformation.

[3]   Faults and fractures are common features of brittlely deformed rocks. Inversion of fault slip data for stress combined with rock mechanics and/or fluid inclusion data have been used to constrain principal stress magnitudes [e.g., *Angelier*, 1989; *André et al.*, 2002]. An alternative approach to quantify stresses is paleopiezometry that relies upon a calibrated relationship between the state of stress and the development of a conspicuous element in the rock. Common paleopiezometers are dislocation density in calcite [e.g., *Pfiffner*, 1982], dynamic recrystallisation of calcite and quartz [e.g., *Twiss*, 1977; *Kohlstedt and Weathers*, 1980] and mechanical twinning in calcite [e.g., *Jamison and Spang*, 1976; *Rowe and Rutter*, 1990; *Lacombe and Laurent*, 1996]. Calcite twinning paleopiezometry provides estimates of maximum differential stresses [e.g., *Lacombe*,

2007], but principal stress magnitudes remain generally out of reach.

[4]   Taking the Laramide-aged Sheep Mountain Anticline (Wyoming, USA) as a case study, we constrain effective principal stress magnitudes in space (across the fold) and time (during the Laramide contraction) using an original combination of published calcite twin data, fault and fracture data and new rock mechanics data. This approach not only provides estimates of stress levels sustained by naturally deforming rocks in the uppermost crust, but also allows evaluation of variations of fluid (over)pressure and/or of syn-folding erosion.

2.   Tectonic Setting

[5]   The Sheep Mountain Anticline is a NW-SE trending basement-cored fold formed above a SW-dipping high angle basement thrust [*Hennier*, 1984; *Stanton and Erslev*, 2004] during the Laramide orogeny (Figures 1a and 1b). The studied sedimentary layers are Permo-carboniferous limestones (Madison and Phosphoria Fms) that were buried down to 2000m below shaly Mesozoic formations before having been fractured and exhumed by folding during the late Cretaceous to Eocene shortening. In the field, the tectonic history of these rocks is witnessed by fractures, stylolites and striated microfaults [e.g., *Bellahsen et al.*, 2006a, 2006b; *Fiore Allwardt et al.*, 2007; *Amrouch et al.*, 2010a]. The sequence of deformation, including a complex layer-parallel shortening (LPS hereafter) history, is well-constrained (Figures 1a, 1d, and 2a). The oldest fracture set (I) strikes 110° to 130° (Figure 2a); it is associated with NE-SW stylolites (Figure 1d) and is interpreted as a pre-Laramide regional set. Set I fractures were left-laterally reactivated during the Laramide stress build-up (LPS 1, Figure 2a). Laramide NW-SE stylolites cut across the pre-Laramide stylolites, the latter being also reopened by set II fractures (Figure 1d) striking ~045° that abut on the tail cracks associated with the shear reactivation of set I fractures. Finally, conjugate sets of newly-formed reverse faults developed, striking parallel to the fold axis, during the last stage of Laramide LPS (LPS 3, Figure 2a), just before anticline growth. Set III joints striking 130° parallel to the fold axis are found mainly along the hinge and formed in response to strata bending during folding. A late stage fold tightening (LSFT hereafter) is marked by strike-slip faults, and by the reactivation of tilted set I fractures as small reverse faults in the forelimb (Figure 2a). Paleostress orientations and differential stress magnitudes related to Laramide LPS and LSFT were determined using the Calcite Stress Inversion technique [*Amrouch et al.*, 2010a]. In contrast to techniques that determine only a 'bulk' differential stress [e.g., *Jamison and Spang*, 1976], which has poor or no meaning in the case of polyphase tectonic evolution [e.g., *Lacombe*, 2010], the

[1]UPMC Sorbonne Universités, UMR 7193, ISTEP, Paris, France.
[2]Geology Geochemistry Geophysics Direction, IFP Energies Nouvelles, Rueil-Malmaison, France.
[3]CNRS, UMR 7193, ISTEP, Paris, France.
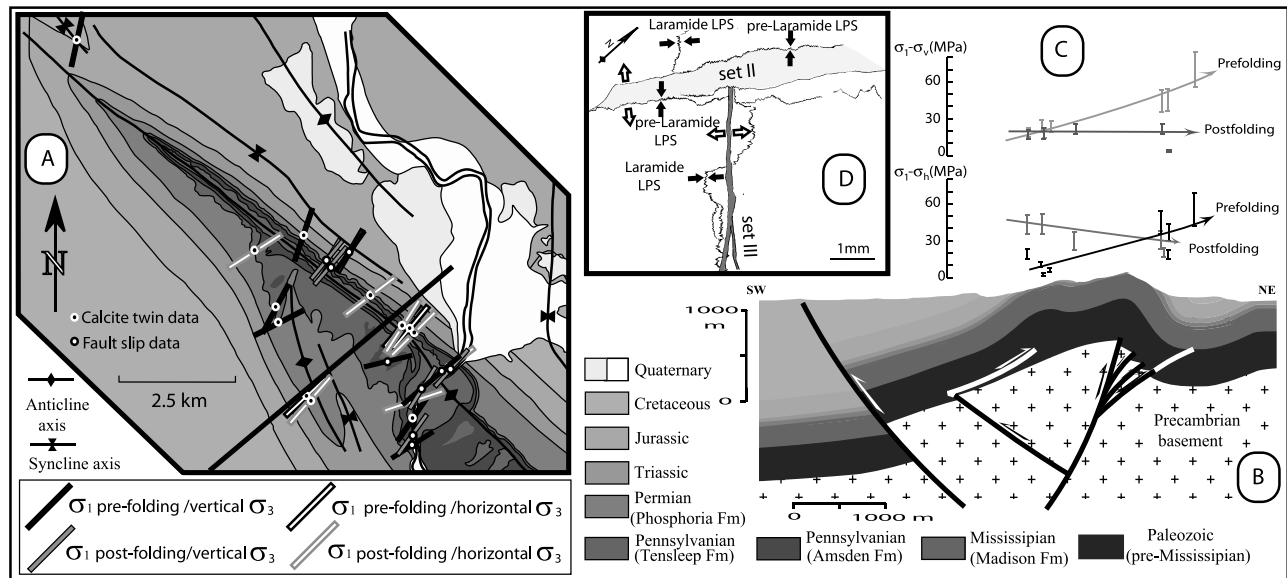
Figure 1. (a) Simplified geological map of the NW part of the Sheep Mountain Anticline with paleo-σ_1 directions reconstructed from fault slip and calcite twin data. (b) Geological cross-section (location in Figure 1a). (c) Evolution of Laramide pre-folding and post-folding differential stresses ($\sigma_1 - \sigma_v$) and ($\sigma_1 - \sigma_h$) across the fold (sites projected perpendicularly on the cross section). Data after *Amrouch et al.* [2010a]. (d) Example of microstructural observations in thin section that constrain the sequence of microstructure development (see text).

CSIT computes simultaneously principal stress orientations and related differential stress magnitudes from sets of mechanically consistent twin data within polyphase samples. This innovative approach allows deciphering the pressure history at Sheep Mountain Anticline. The distinct timing of successive twinning events was delineated first by the observation that some stress tensors have compression axes parallel to bedding dip, and thus correspond to pre-folding stress tensors, while some others have compression axes that are horizontal irrespective of bedding dip thus revealing post-folding stress tensors. We found no clear evidence for tensors with compression axes inclined consistently less than, but in the same direction as bedding dip which would have reflected either synfolding twinning [e.g., *Lacombe*, 2001] or rotation of prefolding twins at the grain scale due to flexural slip [*Harris and Van der Pluijm*, 1998]. The chronology of twinning events is further constrained with respect to fracture development by the comparison of stress tensors recorded in rock matrix and in the successive vein sets.

[6] The first Laramide twinning event, recorded in the matrix and in the cements of set II veins, predated immediately (or occurred at the very onset of) folding and corresponds to a LPS-related contractional stress regime (vertical $\sigma 3$ axis, Figures 1a and 2a). The second twinning event occurred during LSFT under a strike-slip stress regime (vertical $\sigma 2$ axis, Figures 1a and 2a). Both events correspond to a Laramide compression roughly perpendicular to the fold axis (Figure 1a).

[7] Differential stresses ($\sigma_1 - \sigma_v$) and ($\sigma_1 - \sigma_h$) (σ_v: vertical stress, σ_h: minimum horizontal principal stress) are reported in Figure 1c for these two Laramide twinning events. For LPS3, these values are larger in the forelimb (60 and 50 MPa, resp.) than in the backlimb (20 and 10 MPa, resp.). This increase has been tentatively related to stress perturbations in the sedimentary cover at the tip of the

underlying basement fault starting to move during Laramide stress build-up [*Amrouch et al.*, 2010a].

3. How to Quantify Effective Principal Stress Magnitudes?

[8] Paleostress orientations and regimes determined from fractures, calcite twins and faults (Figure 1a) as well as differential stress magnitudes based on calcite twinning paleopiezometry (Figure 1c) were combined with rock mechanics data within a Mohr construction to estimate effective principal stress magnitudes. The method consists of finding the values of σ_1, σ_2 and σ_3 required for consistency between newly formed faulting/fracturing, frictional sliding along preexisting planes (i.e., Byerlee's law), and differential stresses estimated from calcite twinning [*Lacombe and Laurent*, 1992].

[9] To this aim, we run rock mechanics tests to determine the intrinsic failure envelopes of the Phosphoria and Madison formations. Samples were submitted to tension and to compression under confining pressures of 1, 10 and 15/20 MPa, and the deviatoric stresses required for crack development (dilatancy) then macroscopic rock failure were evaluated at each step (auxiliary material, Table S1).[1] We used these data to draw the Mohr circles corresponding to crack development and rock failure and we built the intrinsic envelopes that are tangent to the Mohr circles and define the rock mechanical properties (Figure 2b). We however used in our scenario a mean crack development curve (CDC) for both formations which is a likely better proxy of the brittle strength of the prefractured *in situ* limestones than the failure curve determined
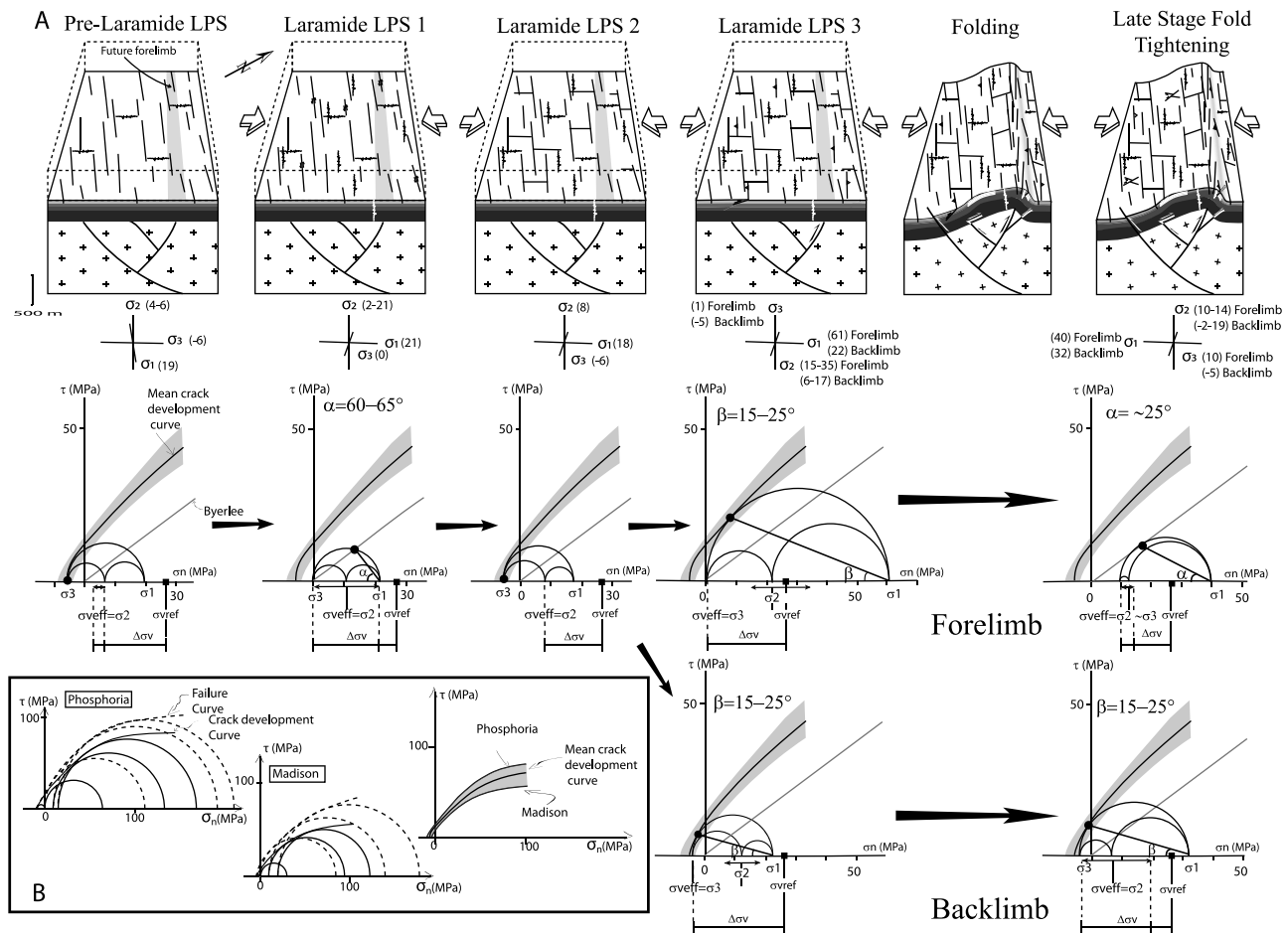
Figure 2. (a) Kinematic and mechanical scenario of development of Sheep Mountain Anticline. For each stage are shown: the microstructures formed, the stress regime and the effective principal stress values (between parentheses) in MPa, and the corresponding Mohr construction. Note that the stress evolution is different in the fold limbs since LPS 3 stage. $\Delta\sigma_v$, σ_{vref} and σ_{veff} are defined in text. For details, see auxiliary material (Tables S1 and S2). (b) Building of crack development curve (continuous circles and line) and failure curve (dashed circles and line) from rock mechanics tests.

from intact present-day rock samples [e.g., *Lacombe*, 2001] (see section 5.2).

4. The Scenario

[10] We define the reference value of the effective vertical principal stress σ_{vref} by considering a pre-folding 2000 m burial of the studied formations and an hydrostatic fluid pressure: $\sigma_{vref} = (\rho - \rho_e)gz$, where ρ and ρ_e are the average densities of the sedimentary overburden and of water (2400 and 1000 kg/m^3, respectively), g is the acceleration of gravity (9.81 ms^{-2}) and z is the depth. We also define $\Delta\sigma_v$ as the difference between σ_{vref} (~27 MPa) and the value of the effective vertical stress σ_{veff} obtained using the Mohr construction. The values of the parameters used and the stress values determined are reported in Table S2 (auxiliary material).

4.1. Pre-Laramide LPS Stage

[11] Effective principal stress magnitudes are constrained by the mode I opening of newly formed set I veins which are vertical and contain σ_2 axis after unfolding, so the (σ_1, σ_3) Mohr circle is tangent to the CDC at a point corresponding to the value of σ_3 (Figure 2a). The maximum differential

stress ($\sigma_1 - \sigma_3$) value is about 25 MPa in both fold limbs (Table S2). Effective principal stress values are $\sigma_1 \sim 19$ MPa and $\sigma_3 \sim -6$ MPa. The nearly 0.5 value of the stress ellipsoid shape Φ ratio $(\sigma_2 - \sigma_3)/(\sigma_1 - \sigma_3)$ (Table S2) leads to $\sigma_2 = \sigma_{veff} \sim 4$–6 MPa.

4.2. Laramide LPS 1

[12] This stage corresponds to the left-lateral shear reactivation of preexisting set I veins (Figure 2a). Because of the absence of newly-formed fractures, the CDC is not reached and the (σ_1, σ_3) Mohr circle and the friction curve ($\tau = 0.85\ \sigma_n$) are secant at the point representing set I fractures that lie at an angle α of 60°–65° to the σ_1 axis (Figure 2a). Effective principal stress values are $\sigma_1 \sim 21$ MPa and $\sigma_3 \sim 0$ MPa. Because of the uncertainty on the Φ ratio, $\sigma_{veff} = \sigma_2$ is poorly constrained, between 2 and 21 MPa (Table S2).

4.3. Laramide LPS 2

[13] The state of stress causes the mode I opening of newly formed set II veins (which are vertical and contain σ_2 axis when unfolded), mainly in the future backlimb and hinge, so the Mohr circle is tangent to the CDC at a point corresponding to the value of σ_3 (Figure 2a). Effective principal stress values are $\sigma_1 = 18$ MPa and $\sigma_3 = -6$ MPa.
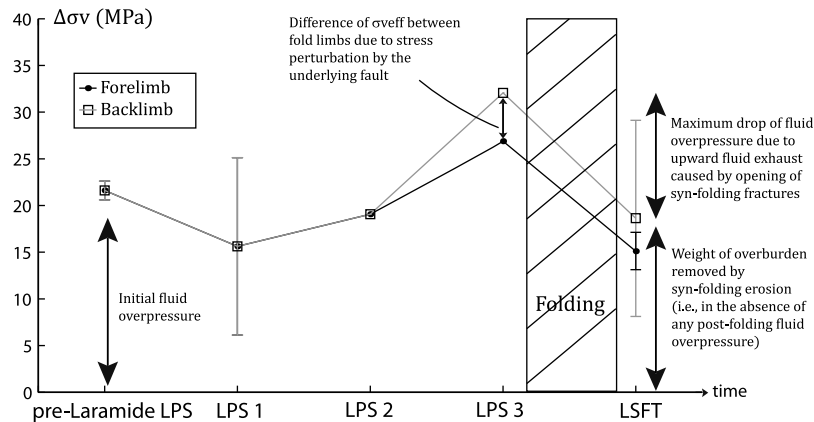
Figure 3. Evolution of the difference $\Delta\sigma_v$ between the reference vertical principal stress σ_{vref} (see text) and the value of σ_{veff} obtained using the Mohr construction at each step, and inferred evolution of the fluid (over)pressure and possible syn-folding erosion. Reported error bars reflect uncertainties on the Φ ratio computed from inversion of calcite twin data.

$\sigma_{veff} = \sigma_2$ is constrained by a single value of the Φ ratio equal to 0.6 (Table S2), which leads to a value of 8 MPa.

4.4. Laramide LPS 3

[14] This stage is associated with the peak differential stress ($\sigma_1 - \sigma_3$) recorded by calcite twinning just before (or at the very onset of) folding. Occurrence at that stage in the forelimb and the backlimb of small-scale newly formed conjugate reverse faults containing σ_2 axis and at an angle β of 15–25° to the σ_1 axis (when unfolded) requires that the (σ_1, σ_3) Mohr circle is tangent to the CDC (Figure 2a). Because strike-slip regimes prevailed earlier (Figure 2a), a permutation between σ_2 and σ_3 axes is needed to account for the evolution toward a contractional regime. Differential stresses reach the mean values of 60 MPa in the forelimb and of 27 MPa in the backlimb (Figure 1c and Table S2). Effective principal stress values are $\sigma_1 = 61$ MPa and $\sigma_3 = \sigma_{veff} = 1$ MPa in the forelimb, and $\sigma_1 = 22$ MPa and $\sigma_3 = \sigma_{veff} = -5$ MPa in the backlimb. The σ_2 value is poorly constrained, between 6 and 17 MPa in the backlimb and between 15 and 35 MPa in the forelimb (Table S2).

4.5. Folding Stage

[15] This stage corresponds to the mode I opening of newly formed set III veins at the fold hinge (Figure 2a). This phase unfortunately lacks significant quantitative constraints on the related extensional state of stress.

4.6. Laramide Late Fold Tightening

[16] In the forelimb, this stage is probably associated with values of σ_2 and σ_3 close to each other (so that σ_2 and σ_3 axes could easily switch between being vertical and horizontal), which would explain how the strike-slip regime recorded by calcite twins caused the compressional reactivation of set I veins as small reverse faults (Figure 2a). For the sake of simplicity, we consider that set I veins were reactivated when making an angle α with σ_1 axis of ~25° (i.e., when tilted in their current attitude), but reactivation may have occurred earlier during folding. Effective principal stress values are $\sigma_1 = 40$ MPa, $\sigma_2 = 12$ MPa and $\sigma_3 = 10$ MPa. In the backlimb, the stress level caused formation of new strike-slip faults (Figure 2a). Effective principal stresses

values are $\sigma_1 = 32$ MPa and $\sigma_3 = -5$ MPa; $\sigma v = \sigma_2$ remains poorly constrained, between -2 and 19 MPa.

5. Discussion

5.1. Assumption of a Vertical Principal Stress Versus Possible Principal Stress Rotations

[17] At all stages of our scenario, one principal stress is considered to be (nearly) vertical throughout the material, independently of the current position within the fold. This assumption is obviously not valid if principal stress directions rotated (e.g., possibly during strata bending). However, our approach does not constrain the attitude of principal stress axes at that stage. Instead, we interpret all the microstructures from the fold limbs as related to either LPS or LSFT. For LSFT, stress tensor computation unambiguously yields a vertical stress axis ($\sigma2$). For LPS2, most set II fractures are clearly pre- (or early-) folding because strata curvature-related set III veins abut on them [*Bellahsen et al.*, 2006a]. It could be argued that reverse microfaults of LPS3, also interpreted to have formed within nearly horizontal strata, could have developed within significantly tilted layers, hence possibly under a non vertical principal stress, if flexural slip occurred at very low friction so that the principal stresses rotated but remained either parallel or perpendicular to bedding. However, several lines of evidence make the occurrence of significant stress rotations at that stage unlikely. First, reverse faults are observed not only in fold limbs where layer-parallel slip is documented by field observations (e.g., in the forelimb [*Sanz et al.*, 2008]), but also at the hinge [*Amrouch et al.*, 2010a] where strata are still nearly horizontal and where outer rim extension prevailed (set III). For a fixed-hinge fold kinematics [*Bellahsen et al.*, 2006b], this is consistent with faulting when the layers were still horizontal or at very low dip. Second, layer-parallel slip at low shear stresses (hence possible large principal stress rotations) is not supported by AMS data showing instead a syn-folding magnetic foliation strongly oblique to the bedding plane in the backlimb [*Amrouch et al.*, 2010b]. As a result, whether the LPS3 microstructures formed in perfectly horizontal layers (strictly pre-folding) or at the very onset of folding within

low dipping strata (early-folding), the assumption of a governing (nearly) vertical principal stress is likely valid.

5.2. Uncertainties on the Effective Principal Stress Values

[18] Estimated effective principal stress values fall in the range of 18 to 61 MPa for σ_1 and −6 to 10 MPa for σ_3, in the limestone strata deformed in the depth range of 1000–2000 m (Figure 3 and Table S2). These values are affected by two main sources of uncertainties. The first one is directly related to the uncertainties on differential stresses estimated by calcite twin analysis (±20%: Figure 1c). The second is induced by the use of the mean CDC to constrain the position of the Mohr circles along the normal stress axis. At the upper crust scale, it is commonly assumed that the strength is limited by the reactivation of well-oriented major discontinuities, i.e Byerlee's law. In contrast, at a local scale within the sedimentary cover where all possible orientations of discontinuities are not available for reactivation, the observation of newly formed fractures and faults reveals the local state of stress at failure. In this case, the CDC is a likely better proxy of the bulk *in situ* brittle strength of the limestones at depth than the failure curve determined from intact present-day rock samples. Note that compared to the general use of Byerlee's curve, the stress derived from the CDC should therefore be considered to provide a minimum value for the least principal stress.

[19] Concerning $\Delta\sigma_v$, the estimate of the burial depth and the hypothesis of one principal stress being vertical are additional causes of uncertainties. Burial depth uncertainties will poorly affect $\Delta\sigma_v$ (a shallower depth of deformation of 300 m will reduce the $\Delta\sigma_v$ of approximately 4 MPa). If one principal stress was not coaxial with gravity (as discussed for LPS3 stage in section 5.1), this will result in an increase of σ_{veff} toward σ_1 and therefore a decrease of $\Delta\sigma_v$. In this case, σ_{veff} can be computed as the normal stress acting on a horizontal plane. With an average 20° dip of the backlimb, an unlikely stress rotation during folding will lead only to a decrease of $\Delta\sigma_v$ of 4 MPa.

[20] As a result, the values obtained should be considered as orders of magnitudes rather than accurate values. Nevertheless, these estimates are amongst the very few available for uppermost crustal paleo-stresses at the particular time of tectonic deformation (e.g., Taiwan [*Lacombe*, 2001]). They are interestingly of the same order than the modern principal stress values determined in strike-slip or compressional stress regimes, *e.g.*, at the SAFOD pilot hole [*Hickman and Zoback*, 2004].

5.3. Evolution of Pore Fluid Pressure and Syn-folding Erosion

[21] Because there is no evidence for erosion or increase of burial before folding, $\Delta\sigma_v$ primarily provides an estimate of the fluid overpressure (Figure 3). During the pre-Laramide stage, $\Delta\sigma_v$ was about 19 MPa (i.e., a fluid pressure of about 38 MPa): this positive value agrees with observations that the fluid pressure is often greater than hydrostatic in orogenic settings [e.g., *Roure et al.*, 2010]. The increase of $\Delta\sigma_v$ (~+13 MPa) during Laramide LPS reflects an increase of the fluid overpressure, the fluid pressure reaching the lithostatic value (~50 MPa) and causing opening of bed-parallel horizontal hydraulic veins. This rise of fluid pressure may be related to the activation of pressure-solution (LPS2) that

reduces porosity and consequently increases pore pressure in limestone strata (Figures 1d and 2a) overlain by Mesozoic shales, which behave as an impermeable barrier for fluids. The difference between the fold limbs is likely related to the perturbation of σ_{veff} at the upper tip of the underlying basement fault [*Bellahsen et al.*, 2006b]. The strong decrease of $\Delta\sigma_v$ during folding (~−15 MPa, Figure 3) could be interpreted as a drop of the fluid pressure related to the development of the bending-related set III veins at the fold hinge. These fractures enhanced vertical permeability of the entire stratigraphic sequence [*Barbier et al.*, 2011], including the impermeable Mesozoic shales, causing an upward fluid exhaust (as suggested by geochemical and fluid inclusion analyses [*Beaudoin et al.*, 2011]) and a subsequent major drop of the fluid pressure.

[22] If the entire fluid overpressure was released at that stage, it is possible to derive the maximum value of syn-folding erosion (Figure 3). This value is poorly constrained in the backlimb (580–2000 m) but is estimated more accurately in the forelimb (950 m–1250 m). Since a large difference in syn-folding erosion between fold limbs is unlikely, ~1000 m of syn-folding erosion is a reasonable estimate. The removal of the remaining burial therefore occurred after the end of the main Laramide event.

6. Conclusions

[23] This study provides an original attempt at combining microstructural data with rock mechanics data to constrain the stress levels sustained by sedimentary rocks deformed by folding in the uppermost crust. Beyond regional implications, it offers a promising way to access effective paleo-principal stress magnitudes, changes in fluid (over)pressure and even estimates of denudation, to be used as inputs in realistic numerical models of thrust belts and foreland basins.

References

Amrouch, K., O. Lacombe, N. Bellahsen, J. M. Daniel, and J. P. Callot (2010a), Stress/strain patterns, kinematics and deformation mechanisms in a basement-cored anticline: Sheep Mountain Anticline (Wyoming, USA), *Tectonics*, *29*, TC1005, doi:10.1029/2009TC002525.

Amrouch, K., P. Robion, J.-P. Callot, O. Lacombe, J.-M. Daniel, N. Bellahsen, and J.-L. Faure (2010b), Constraints on deformation mechanisms during folding based on rock physical properties: Example of Sheep Mountain Anticline (Wyoming, USA), *Geophys. J. Int.*, *182*, 1105–1123, doi:10.1111/j.1365-246X.2010.04673.x.

André, A. S., J. Sausse, and M. Lespinasse (2002), A new method for the quantification of paleostress magnitudes: Sequential sealing of the Soultz-sous-Forêt vein system (Rhine graben, France), *Tectonophysics*, *336*, 215–231.

Angelier, J. (1989), From orientation to magnitudes in paleostress determinations using fault slip data, *J. Struct. Geol.*, *11*(1–2), 37–50, doi:10.1016/0191-8141(89)90034-5.

Barbier, M., J. P. Callot, J. M. Daniel, and Y. Hamon (2011), The sedimento-diagenetic control on the multiscale fracturing of a carbonate reservoir, the Madison Formation (Sheep Mountain, Wyoming, USA), *Geophys. Res. Abstr.*, *13*, EGU2011.

Beaudoin, N., N. Bellahsen, O. Lacombe, and L. Emmanuel (2011), Fracture-controlled paleohydrogeology in a basement-cored, fault-related fold:

Sheep Mountain Anticline (Wyoming, USA), *Geochem. Geophys. Geosyst.*, *12*, Q06011, doi:10.1029/2010GC003494.

Bellahsen, N., P. Fiore, and D. D. Pollard (2006a), The role of fractures in the structural interpretation of Sheep Mountain Anticline, Wyoming, *J. Struct. Geol.*, *28*(5), 850–867, doi:10.1016/j.jsg.2006.01.013.

Bellahsen, N., P. Fiore, and D. D. Pollard (2006b), From spatial variation of fracture patterns to fold kinematics: A geomechanical approach, *Geophys. Res. Lett.*, *33*, L02301, doi:10.1029/2005GL024189.

Fiore Allwardt, P., N. Bellahsen, and D. D. Pollard (2007), Curvature and fracturing based on global positioning system data collected at Sheep Mountain Anticline, Wyoming, *Geosphere*, *3*, 408–421, doi:10.1130/GES00088.1.

Harris, J. H., and B. A. Van der Pluijm (1998), Relative timing of calcite twinning strain and fold-thrust belt development: Hudson Valley fold-thrust belt, New York, USA, *J. Struct. Geol.*, *20*(1), 21–31, doi:10.1016/S0191-8141(97)00093-X.

Hennier, J. H. (1984), Structural analysis of the Sheep Mountain anticline, Bighorn basin, Wyoming, MS thesis, 118 pp., Tex. A&M Univ., College Station.

Hickman, S., and M. D. Zoback (2004), Stress orientations and magnitudes in the SAFOD pilot hole, *Geophys. Res. Lett.*, *31*, L15S12, doi:10.1029/2004GL020043.

Jamison, W. R., and J. H. Spang (1976), Use of calcite twin lamellae to infer differential stresses, *Geol. Soc. Am. Bull.*, *87*, 868–872, doi:10.1130/0016-7606(1976)87<868:UOCTLT>2.0.CO;2.

Kohlstedt, D. L., and M. S. Weathers (1980), Deformation-induced microstructures, paleopiezometers and differential stress in deeply eroded fault zones, *J. Geophys. Res.*, *85*, 6269–6285, doi:10.1029/JB085iB11p06269.

Lacombe, O. (2001), Paleostress magnitudes associated with development of mountain belts: Insights from tectonic analyses of calcite twins in the Taiwan Foothills, *Tectonics*, *20*(6), 834–849, doi:10.1029/2001TC900019.

Lacombe, O. (2007), Comparison of paleostress magnitudes from calcite twins with contemporary stress magnitudes and frictional sliding criteria in the continental crust: Mechanical implications, *J. Struct. Geol.*(1), *29*, 86–99, doi:10.1016/j.jsg.2006.08.009.

Lacombe, O. (2010), Calcite twins, a tool for tectonic studies in thrust belts and stable orogenic forelands, *Oil Gas Sci. Technol.*, *65*(6), 809–838, doi:10.2516/ogst/2009088.

Lacombe, O., and P. Laurent (1992), Determination of principal stress magnitudes using calcite twins and rock mechanics data, *Tectonophysics*, *202*, 83–93, doi:10.1016/0040-1951(92)90456-G.

Lacombe, O., and P. Laurent (1996), Determination of deviatoric stress tensors based on inversion of calcite twin data from experimentally deformed monophase samples: Preliminary results, *Tectonophysics*, *255*, 189–202, doi:10.1016/0040-1951(95)00136-0.

Pfiffner, O. A. (1982), Deformation mechanisms and flow regimes in limestones from the Helvetic zone of the Swiss Alps, *J. Struct. Geol.*, *4*(4), 429–442, doi:10.1016/0191-8141(82)90034-7.

Roure, F., et al. (2010), The use of paleo-thermo-barometers and coupled thermal, fluid flow and pore-fluid pressure modelling for hydrocarbon and reservoir prediction in fold-thrust belts, *Geol. Soc. Spec. Publ.*, *348*, 87–114.

Rowe, K. J., and E. H. Rutter (1990), Paleostress estimation using calcite twinning: Experimental calibration and application to nature, *J. Struct. Geol.*, *12*(1), 1–17, doi:10.1016/0191-8141(90)90044-Y.

Sanz, P. F., D. D. Pollard, P. F. Allwardt, and R. I. Borja (2008), Mechanical models of fracture reactivation and slip on bedding surfaces during folding of the asymmetric anticline at Sheep Mountain, Wyoming, *J. Struct. Geol.*, *30*(9), 1177–1191, doi:10.1016/j.jsg.2008.06.002.

Stanton, H. I., and E. A. Erslev (2004), *Sheep Mountain Anticline: Backlimb tightening and sequential deformation in the Bighorn Basin, Wyoming, 53rd Guidebook*, pp. 75–87, Wyo. Geol. Assoc., Casper.

Twiss, R. J. (1977), Theory and applicability of a recrystallized grain size paleopiezometer, *Pure Appl. Geophys.*, *115*, 227–244, doi:10.1007/BF01637105.

K. Amrouch, N. Beaudoin, N. Bellahsen, and O. Lacombe, UPMC Sorbonne Universités, UMR 7193, ISTEP, F-75005, Paris, France.

J.-M. Daniel, Geology Geochemistry Geophysics Direction, IFP Energies Nouvelles, F-92852 Rueil-Malmaison, France.